Interaction Analysis of Virtual Synchronous Machine Control with the AC Grid

Jesús F. Huaman*, Jose Carlos U. Pena†, Daniel Dotta*, Reinaldo Tonkoski‡

* Universidade Estadual de Campinas, Campinas, Brazil

Emails: j264534@unicamp.br, dottad@unicamp.br

† KEMA Laboratories, Arnhem, The Netherlands

Emails: jose.ugaz@kema.com

‡Technical University of Munich, Munich, Germany

Email: reinaldo.tonkoski@tum.de

***Abstract*—Virtual Synchronous Machine (VSM) controllers are regarded as a promising Grid-Forming solution for the large-scale integration of renewable generation, due to their ability to emulate the behavior of synchronous machines. Numerous studies have shown that VSM enhance stability in weak grids; however, little attention has been paid to potential instability issues when Virtual Impedance (VI) and multiple control loops are employed under varying grid conditions. This paper analyzes the stability of a VSM with VI using the multiple-input multiple-output (MIMO) transfer function and Singular Value Decomposition (SVD), explicitly considering variations in grid impedance. The study reveals how the interaction between VI and grid impedance can lead to subsynchronous oscillations in weak grids and high-frequency resonances in strong grids. Based on these findings, a guide for tuning the VI is proposed. The validity of the analysis is confirmed through experimental tests in a Control Hardware-in-the-Loop (C-HIL) environment.**

***Index Terms*—Virtual Synchronous Machine (VSMs), Singular Value Decomposition (SVD), Control Hardware in the Loop (C-HIL).**

I. Introduction

The increasing penetration of renewable energy sources (RES) is changing the traditional operation paradigm of power systems [1]. An ever larger share of generation is interfaced through power electronic converters, and system operators now require these device to actively support grid voltage and frequency [2]. Among the proposed control strategies, the Virtual Synchronous Machine (VSM) concept has emerged as a key solution, as it can emulate inertia and enhance the dynamic frequency and voltage response at the point of common coupling (PCC).

Most existing studies show that VSM significantly improve stability in weak grids, where Grid-Following (GFL) converters may fail to operate reliably [3]–[5]. However, much less attention has been paid to the behavior of multi-loop VSM with virtual impedance when connected to stiff grids. Analyzing stability in such operating conditions is crucial for understanding the underlying mechanisms and for providing suitable design criteria to system operators. For example, [6] compares the small-signal stability of GFL and GFM converters using state-space models (SSM), but does not clearly explain the origin of the unstable modes it identifies. The works in [3], [4] propose design guidelines for VSM virtual impedance in weak grids, but they do not consider full multi-loop control structures. Other studies, e.g., [7], [8], analyze the interaction between GFM converters and the grid, yet they do not explicitly address multi-loop VSMs with virtual impedance.

Building on the previous works, the main objective of this paper is to analyze how VI interacts with grid impedance and how this interaction can lead to instability in strong grids. The main contributions are summarized as follows:

- A detailed characterization of the interaction between VI and grid impedance using a MIMO transfer-function model of the VSM and SVD, which reveals how control and grid dynamics couple across different grid strength.
- A practical design guideline is developed for tuning l_v and r_v to improve the stability margins of VSMs over a wide range of grid conditions.
- The proposed analysis is validated through C-HIL experiment, confirming that the predicted instability mechanisms and stability trends are consistently observed in practice.

The remainder of this paper is organized as follows. Section II introduces the system under study, the VSM-based control architecture, and the eigenvalue analysis. Section III presents the SVD-based characterization of the converter–grid interaction. Section IV proposes a design guideline for the virtual impedance. Section V discusses the experimental validation in a C-HIL environment. Finally, Section VI provides the conclusions and outlines directions for future work.

II. Application Overview

A. System Description

Fig. 1 shows the electrical and control architecture of a battery fed converter connected to a power grid. The inverter provide voltage support and virtual inertia to the grid by emulating the dynamic behavior of a synchronous machine. The grid side converter is connected to the point of common coupling (PCC) trough an L_f, C_f, L_c filter. The grid-side current i_o and the capacitor voltage v_o are measured and used in the control loops. A synchronous reference frame (SRF) aligned with the inverter output v_b^{dq} is adopted for

979-8-3315-8138-1

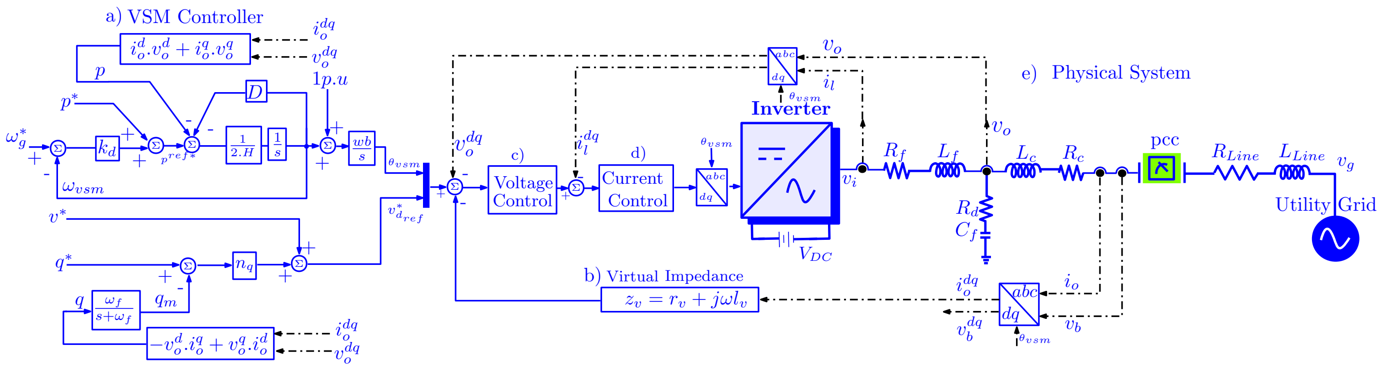

Fig. 1: Block diagram showing the link between the VSM and the network small-signal model.

the implementation of the inner control loops. The outer VSM-based control layer regulates active and reactive power and generates the voltage reference for the converter. This multilayer structure, together with the LCL filter, the VI, and the grid impedance, defines the overall VSM-filter-grid dynamics that will be captured in the SSM.

B. Small-Signal Modeling Methodology for VSM

Starting from the nonlinear model of the system in Fig. 1, the SSM of the VSM is developed following the methodology described in [8], [9]. The model captures the dynamic interactions between the VSM control layers, the power stage (LCL filter), the virtual impedance, and the grid impedance, providing a unified representation of the complete system. For the stability analysis, all dynamic equations are expressed in a common DQ reference frame aligned with the grid voltage vector v_g, whereas the internal dynamics of the VSM are formulated in a local dq frame aligned with the converter output voltage. The transformation between these two frames is given by:

$$\left[f_{DQ}\right] = \begin{bmatrix} \cos(\delta) & -\sin(\delta) \\ \sin(\delta) & \cos(\delta) \end{bmatrix} \left[f_{dq}\right] \tag{1}$$

where f represents an electrical quantity (e.g., voltage or current), and δ is the angular difference between the VSM voltage vector and the ideal grid voltage.

The complete linearized SSM of the VSM and grid-connected system is compactly represented as:

$$\Delta\dot{\mathbf{x}}_{sys} = A_{mg}\,\Delta\mathbf{x}_{sys} + B_{mg}\,\Delta\mathbf{u}_{sys} \tag{2}$$

$$\Delta\mathbf{y}_{sys} = C_{mg}\,\Delta\mathbf{x}_{sys} + D_{mg}\,\Delta\mathbf{u}_{sys} \tag{3}$$

where:
$A_{mg} \in \mathbb{R}^{19\times19}$, $B_{mg} \in \mathbb{R}^{19\times5}$, $C_{mg} \in \mathbb{R}^{2\times19}$, $D_{mg} \in \mathbb{R}^{2\times5}$

where $\Delta(\cdot)$ denotes small-signal deviations from steady state. The state vector $\Delta\mathbf{x}_{sys}$ includes the VSM internal states, filter dynamics, and network variables, and is given by:

$$\Delta\mathbf{x}_{sys} = \big[\Delta\omega_{vsm}, \Delta\theta_{vsm}, \Delta Q, \Delta\phi^{dq}, \Delta\gamma^{dq}, \Delta X^{1234}, \Delta i_l^{dq}, \Delta v_o^{dq}, \Delta i_o^{dq}, \Delta i_{NET}^{DQ}\big]^T$$

The detailed definition and modeling of these state variables can be found in previous work [9] with the addition in this work of a second order Padé approximation to account for control delay dynamics (ΔX^{1234}). The input vector is given by:

$$\Delta\mathbf{u}_{sys} = \left[\Delta p^*, \Delta q^*, \Delta V_g^D, \Delta V_g^Q, \Delta\omega_g^*\right]^T$$

representing the reference active/reactive powers, the grid voltage components in the DQ frame, and the nominal grid frequency.

In this framework, the matrices A_{mg},B_{mg},C_{mg},D_{mg} capture the full linearized dynamics of the closed loop system. These will be used for classical small signal stability via eigenvalue computation in the next subsection. The Table I the show the controller and VSM parameters.

TABLE I: VSM parameters and controller gains

Parameter	Variable	Value
Rated voltage	V_n	380 V
Base voltage	V_b	310.2687 V
Rated (base) Power	S_b	50 KVA
Rated (base) frequency	f_b	60 Hz
Switching frequency	f_{sw}	20 kHz
Base impedance	Z_b	2.88 Ω
Voltage DC Link	V_{DC}	800 V
Base current	I_b	107.4338 A
Base inductance	L_b	0.0077 H
Base capacitance	C_b	$9.1848e-04$ F
Filter Inductance	L_f, l_f	1 mH, 0.1305 p.u
Filter Capacitance	C_f, c_f	100 μF, 0.1089 p.u
Filter Inductance output	L_c, l_c	50 μH, 0.0065 p.u
Simulation step		1 μs
Sampling frequency		20 kHz
Current control gains	k_{pc}, k_{ic}	$2.1758, 100$
Voltage control gains	k_{pv}, k_{iv}	$0.36, 200$
Virtual inductante	l_v	0.2
Virtual Resistance	r_v	0.1
Virtual inertia gains	H, D, k_d	$2, 30, 20$
$q-v$ droop loop	ω_q, n_q	$1000, 0.5$

C. Eigenvalue analysis

In this section, parametric eigenvalue sweeps are carried out with respect to both the grid impedance and the VSM virtual impedance. The line parameters are varied in the ranges $L_{line} \in [0.3, 0.02]$ p.u. (i.e., $L_{line} \in [2.3, 0.15]$ mH) and $R_{line} \in [3.5\times10^{-4}, 0.17]$ p.u. (i.e., $R_{line} \in [1\times10^{-3}, 0.5]$ Ω), while the virtual inductance and resistance are swept in $l_v \in [0, 0.5]$ p.u. and $r_v \in [0, 0.5]$ p.u., respectively.

979-8-3315-8138-1

Fig. 2(a) shows that reducing the line inductance from a weak to a stiff grid (L_{line} : 2.3 mH $\rightarrow$ 0.15 mH) mainly affects the high-frequency poles, which move towards the imaginary axis and may cross into the right half-plane, thus compromising stability. In contrast, Fig. 2(b) illustrates that increasing the line resistance (R_{line} : 1m $\Omega \rightarrow 0.5$ Ω) under a predominantly inductive grid (L_{line} = 1 mH) produces only minor changes in the eigenvalues, indicating that grid inductance has a much stronger impact on the VSM dynamics than grid resistance.

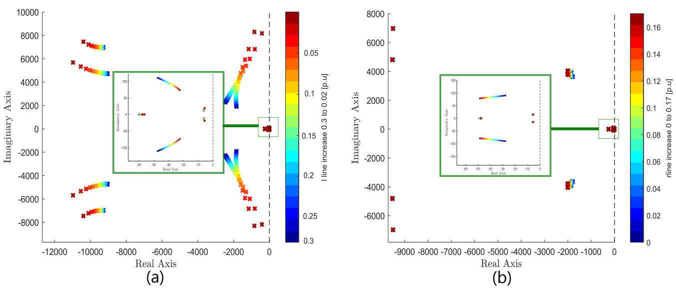

Fig. 2: Closed-loop eigenvalue loci under different line impedances: (a) decreasing l_{line} from 0.3 to 0.02 p.u.; (b) increasing r_{line} from 0 to 0.17 p.u.

Fig. 3(a) and Fig. 3(b) show the effect of sweeping the virtual inductance and resistance, respectively. Increasing l_v (with fixed r_v = 0.1 p.u.) enhances the damping of the subsynchronous modes with only a slight influence on the kHz-range poles, whereas increasing r_v (with fixed l_v = 0.2 p.u.) further improves the damping of subsynchronous modes with negligible changes in high-frequency poles (for L_{line} = 1 mH, R_{line} = 1 Ω). Overall, these results highlight that line inductance predominantly shapes the high-frequency dynamics, while the virtual resistance is the main lever to control subsynchronous eigenvalues.

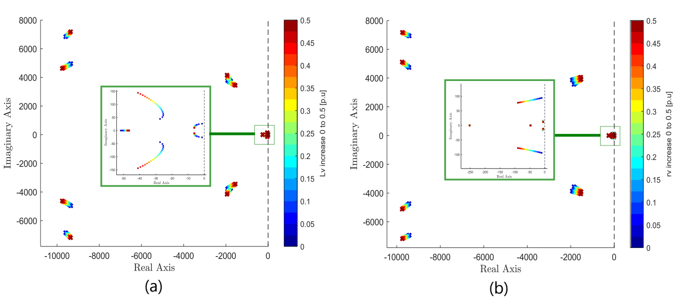

Fig. 3: Closed-loop eigenvalue loci under different virtual impedance settings: (a) increasing virtual inductance l_v from 0 to 5 p.u.; (b) increasing virtual resistance r_v from 0 to 0.5 p.u. for the same inductive grid.

III. Singular Value Decomposition Analysis

While the eigenvalue study in the previous subsection characterizes the location and damping of the system modes, it does not quantify how strongly each mode is excited by different inputs or observed at different outputs. To capture these directional properties in the frequency domain, we employ the SVD of the MIMO transfer function.

A. Mathematical Formulation of the SVD

The SVD is widely used in control engineering to analyze the directional gain of MIMO systems in the frequency domain; a detailed presentation can be found in [10]. Let $G(j\omega) \in \mathbb{C}^{p\times m}$ denote the MIMO transfer matrix of the system in the frequency domain. For each frequency ω, its singular value decomposition is given by:

$$G(j\omega) = U(j\omega)\,\Sigma(j\omega)\,V^H(j\omega), \tag{4}$$

where $U(j\omega) \in \mathbb{C}^{p\times p}$ and $V(j\omega) \in \mathbb{C}^{m\times m}$ are unitary matrices, and

$$\Sigma(j\omega) = \operatorname{diag}\big(\sigma_1(\omega), .., \sigma_q(\omega)\big), \quad \sigma_1(\omega) \geq .. \geq \sigma_q(\omega) \geq 0 \tag{5}$$

with $q = \min(p, m)$ and $\sigma_i(\omega)$ the singular values of $G(j\omega)$.

The largest singular value,

$$\sigma_{\max}(\omega) := \sigma_1(\omega) = \max_{u\neq 0} \frac{\|G(j\omega)u\|_2}{\|u\|_2}, \tag{6}$$

represents the maximum gain of the system at frequency ω. The corresponding right and left singular vectors, $v_1(j\omega)$ (column of V) and $u_1(j\omega)$ (column of U), define the input and output directions, respectively, along which this maximum gain is attained:

$$G(j\omega)\,v_1(j\omega) = \sigma_{\max}(\omega)\,u_1(j\omega). \tag{7}$$

This formulation is commonly employed to assess directional gain, loop coupling, and robustness to disturbances in MIMO control systems. In this context, the SVD is applied to the SSM of the VSM–network system given in (2)–(3), whose transfer matrix is:

$$G(s) = C_{mg}(sI - A_{mg})^{-1}B_{mg} + D_{mg}, \quad s = j\omega, \tag{8}$$

where the number of outputs (e.g., network currents), and the number of inputs (e.g., Δp^*, Δq^*, ΔV_g^D, ΔV_g^Q, $\Delta\omega_g^*$). As defined in (4), the frequency-dependent quantity

$$\sigma(\omega) := \sigma_{\max}\big(G(j\omega)\big) \tag{9}$$

represents the maximum gain from any input direction to any output direction at frequency ω and is used as a frequency dependent sensitivity metric. This enables the detection of resonances that may not be observable from eigenvalue analysis alone and facilitates VI tuning by identifying frequency regions with poor damping.

B. Singular Value Decomposition Analysis of System

Based on this formulation, Fig. 4 shows the maximum singular value $\sigma_{\max}(\omega)$ and the input participation in its direction. The curve $\sigma_{\max}(\omega)$ exhibits a pronounced peak of about $40,\mathrm{dB}$ around $1–3,\mathrm{Hz}$, revealing a poorly damped low–frequency mode associated with the VSM power–frequency coupling, whereas the smaller resonance of roughly $5,\mathrm{dB}$ at a few hundred hertz indicates better damping of the LCL and current–loop modes.

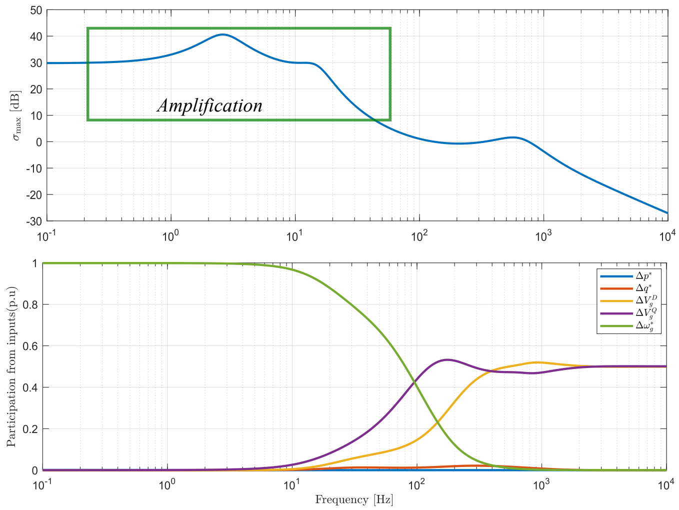

Fig. 4: Frequency response of the maximum SV and the participation of the inputs

The input–participation analysis shows that, at low frequencies ($< 10,\mathrm{Hz}$), the critical dynamics are dominated by grid–frequency perturbations $\Delta\omega_g^*$. For intermediate frequencies (10–200, Hz), the maximum gain is mainly driven by grid–voltage variations, predominantly along the q axis, while around $10^3,\mathrm{Hz}$ it results from a combination of ΔV_g^D and ΔV_g^Q. Active and reactive power setpoints have negligible influence over the entire frequency range, indicating that robustness is primarily limited by grid–induced perturbations rather than by changes in power references.

C. Impact of Grid and Virtual Impedance

Fig. 5 shows the sensitivity of the VSM to grid parameters through the frequency response of the maximum SV $\sigma_{\max}(\omega)$ when the grid inductance l_{line} and resistance r_{line} are varied. Two dominant features appear in Fig. 5(a): a low–frequency peak around 1–3 Hz, associated with the VSM power–frequency coupling, and a high–frequency resonance in the 1–2 kHz range, linked to the LCL filter and current–loop dynamics. As the grid becomes weaker (larger l_{line}), the low–frequency peak of $\sigma_{\max}(\omega)$ grows, indicating higher sensitivity to slow grid disturbances, while the high–frequency resonance is attenuated. Conversely, for stiff grids (e.g., $L_{line} \approx 0.15\,\mathrm{mH}$), the resonance around 1–2 kHz becomes more pronounced and can interact with the current controller, a risk that is not fully evident from eigenvalue loci alone. Fig. 5(b) further shows that increasing r_{line} has little effect at low frequency but provides additional damping in the mid and high frequency ranges, reducing the amplitude of the resonant peaks; physically, the grid resistance acts as a damping term for the LCL and current–loop dynamics.

Fig. 6 illustrates how the virtual impedance reshapes these behaviours and directly interacts with the grid impedance. Increasing the virtual inductance l_v (Fig. 6(a)) shifts the subsynchronous resonance towards lower frequencies and reduces its magnitude, while leaving the kHz-range resonance almost unchanged; this indicates that l_v mainly modifies the effective output impedance seen at low frequencies, altering how the VSM shares power and reacts to slow grid variations. In contrast, adding virtual resistance r_v (Fig. 6(b)) provides effective damping of the low frequency peak and smooths the mid frequency response without significantly affecting the high–frequency resonance. From a physical standpoint, the line inductance sets the natural resonance between the grid and the LCL filter, whereas the virtual resistance controls how strongly that resonance is excited and how subsynchronous oscillations are damped. The SVD based analysis makes this separation of roles and the coupling between grid and virtual impedance explicitly visible in the frequency domain, highlighting critical interaction mechanisms that are much harder to interpret from eigenvalue plots alone.

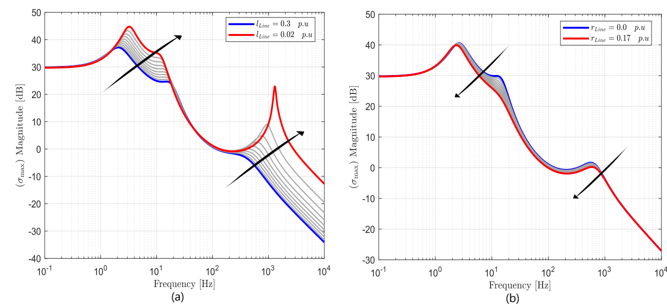

Fig. 5: Frequency response of the maximum singular value $\sigma_{\max}(\omega)$ when (a) grid inductance varies (l_{line}) and (b) grid resistance varies (r_{line}).

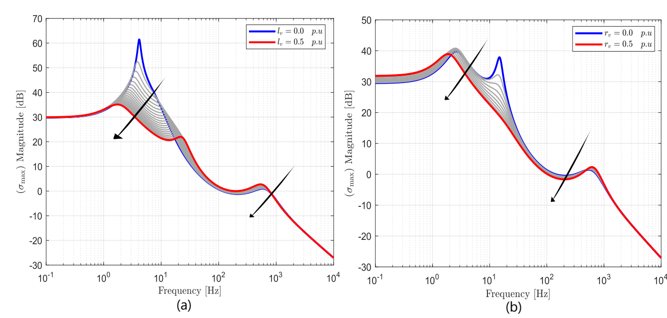

Fig. 6: Frequency response of the maximum singular value $\sigma_{\max}(\omega)$ when (a) virtual inductance varies (l_v) and (b) virtual resistance varies (r_v).

IV. Guideline for tuning l_v and r_v

This section outlines a concise procedure to select the virtual impedance parameters r_v and l_v in VSMs, combining small-signal and frequency-domain analysis.

1) **Set core VSM parameters:** Choose H, D, K_d, n_q according to grid-code requirements and desired dynamic response.
2) **Obtain the linear model:** Derive the full small-signal state-space model including control loops, LCL filter, virtual impedance, and grid interface.

979-8-3315-8138-1

3) **Check eigenvalue stability:** Evaluate closed-loop eigenvalues over a range of grid impedances to identify critical low- and high-frequency modes.
4) **Run SVD analysis:** Compute $\sigma_{\max}(G(j\omega))$ and input–output participation to locate resonant peaks and their dominant excitation directions.
5) **Select r_v, l_v:** Choose r_v and l_v that reduce high-frequency gain and improve subsynchronous damping, ensuring acceptable performance for both weak and stiff grids.
6) **Validate in C-HIL:** Implement the selected parameters in a C-HIL setup and confirm that the measured response matches the predicted damping and robustness.

V. C-HIL Validation

To validate the analysis in section III, C-HIL experiments were carried out using a real time simulator and a physical micro-controller running the VSM controller. Fig. 7 shown the HIL setup used in the tests.

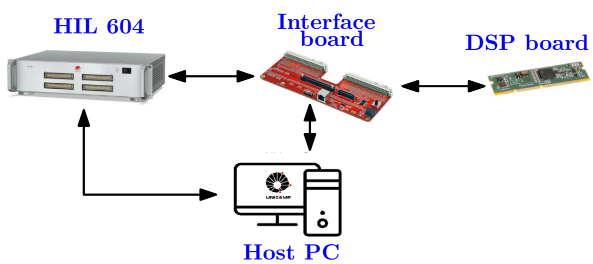

Fig. 7: Hardware in the Loop setup for simulation results

Fig. 8, demonstrate that the SVD analysis correctly predicts high-frequency resonances, a C-HIL test is performed in which the grid inductance is stepped from a weak-grid condition (L_{line} = 1 mH) to a stiff grid (L_{line} = 0.1 mH), while keeping the controller gains unchanged. The test starts from an operating point with $r_v = 0.1$ p.u., $l_v = 0.2$ p.u., $L_{line} = 1$ mH, and $R_{line} = 1$ mΩ. When the grid is made stiff, the C-HIL experiment shows the almost instantaneous onset of a 2 kHz oscillation that drives the system to instability, in agreement with the resonance predicted by the SVD-based analysis.

VI. Conclusion

The main contribution of this work is the combination of a Small Signal Model with Singular Value Decomposition to assess instability risk in VSM with virtual impedance under varying grid conditions. The joint use of eigenvalue and SVD analysis enables not only the localization of critical low and high frequency modes but also the identification of input-output directions that most strongly excite them, thereby providing a more interpretable assessment of stability. The validity of the proposed framework has been confirmed by experiments in a Control Hardware in the Loop environment.

Future work will focus on extending the proposed framework in the following directions:

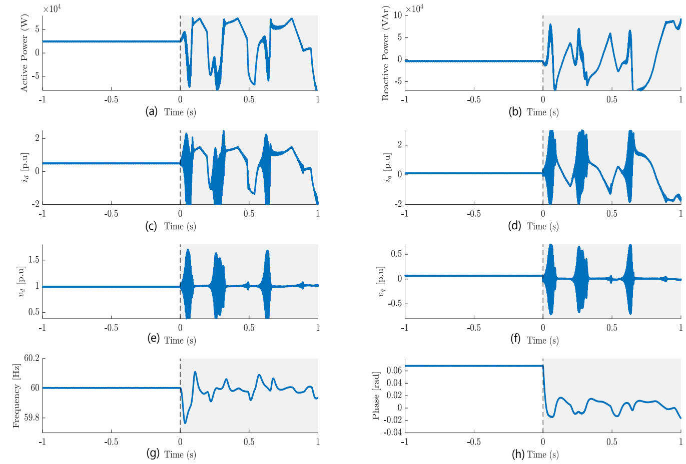

Fig. 8: CHIL test result

- Small signal stability analysis of multiple GFM and GFL units operating in parallel, connected through resistive and mixed (R-L) network impedance, to assess interaction modes and possible resonance mechanisms in larger converter-dominated systems
- Investigation for coupling effect of Active and Reactive Power Control on stability of VSM.

References

[1] J. F. Huaman, L. E. dos Santos, J. I. Y. Ota, J. F. Guerreiro, and D. Dotta, "Análise dinâmica da campusgrid: Microrrede na universidade estadual de campinas (unicamp)," *Simpósio Brasileiro de Sistemas Elétricos-SBSE*, vol. 2, no. 1, 2022.

[2] Y.-K. Wu, S.-M. Chang, and P. Mandal, "Grid-connected wind power plants: A survey on the integration requirements in modern grid codes," *IEEE Transactions on Industry Applications*, vol. 55, no. 6, pp. 5584–5593, 2019.

[3] A. Rodriguez-Cabero, J. Roldán-Pérez, and M. Prodanovic, "Virtual impedance design considerations for virtual synchronous machines in weak grids," *IEEE Journal of Emerging and Selected Topics in Power Electronics*, vol. 8, no. 2, pp. 1477–1489, 2019.

[4] J. Roldán-Pérez, A. González-Cajigas, A. Rodríguez-Cabero, M. Prodanovic, and P. Zumel, "Design and analysis of a current-controlled virtual synchronous machine for weak grids," in *2019 IEEE Applied Power Electronics Conference and Exposition (APEC)*. IEEE, 2019, pp. 1459–1465.

[5] Z. Hu, X. Xing, H. Wang, Z. Li, Y. Li, and F. Blaabjerg, "Modeling and delay compensation method for improving the stability of grid-connected inverter with lcl filter under weak grid conditions," *IEEE Transactions on Power Electronics*, pp. 1–12, 2025.

[6] X. Gao, D. Zhou, A. Anvari-Moghaddam, and F. Blaabjerg, "Stability analysis of grid-following and grid-forming converters based on state-space modelling," *IEEE Transactions on Industry Applications*, vol. 60, no. 3, pp. 4910–4920, 2024.

[7] J. F. Huaman, L. E. Dos Santos, J. C. Ugaz, and D. Dotta, "A comparative analysis of grid-following and grid-forming converters with hil validation," in *2025 IEEE Power & Energy Society General Meeting (PESGM)*. IEEE, 2025, pp. 1–5.

[8] J. F. Huaman, L. E. dos Santos, J. C. Ugaz Pena, J. A. Pomilio, and D. Dotta, "Seamless transitions between grid-tied and islanded operation in a brazilian microgrid," in *2024 IEEE Power Energy Society General Meeting (PESGM)*, 2024, pp. 1–5.

[9] J. F. Huaman, L. E. Dos Santos, J. C. U. Peña, and R. Tonkoski, "State-space modeling and c-hil validation of a vsm: Virtual-resistance effects across grid strengths," *Authorea Preprints*, 2025.

[10] W. S. Levine, *The Control Systems Handbook: Control System Advanced Methods*. CRC press, 2018.

979-8-3315-8138-1